A FUNDAMENTAL STUDY OF THE PERFORMANCE OF X-SECTION CAST-IN-PLACE CONCRETE SINGLE PILES

Yu Wang
PLA University of Science and Technology,
State Key Laboratory of Disaster Prevention & Mitigation of Explosion & Impact
Nanjing 210007, China
E-mail: lgdxwangyu@163.com

Yaru Lv
PLA University of Science and Technology,
State Key Laboratory of Disaster Prevention & Mitigation of Explosion & Impact
Nanjing 210007, China
E-mail: yaru419828@163.com

Dongdong Zhang *(corresponding author)*
PLA University of Science and Technology,
College of Field Engineering
Nanjing 210007, China
E-mail: zhangdodo_163@163.com

Jieying Zhou
PLA University of Science and Technology,
College of Defense Engineering
Nanjing 210007, China
E-mail: zhoujieying666@126.com

Abstract

X-section cast-in-place concrete (XCC) piles are used because they have a higher bearing capacity than circular-section cast-in-place concrete (CCC) piles of the same cross-sectional area. Although the bearing capacity of XCC piles has been studied, the performance of XCC single piles, especially for the stress-transfer mechanism dependent on the geometrical effects, is still not fully understood. This paper reports two comparative field static load tests on an XCC and a CCC single pile of the same cross-sectional area. In addition, corresponding three-dimensional numerical back-analyses are performed to provide a fundamental understanding. The measured and computed results reveal that the XCC single pile has an approximately 25% higher ultimate bearing capacity than the CCC single pile. This is because the XCC single pile has an approximately 20% larger total side resistance, which is caused by a 60% larger pile perimeter and a slightly smaller unit side resistance. Lateral soil arching effects are developed, causing a non-uniform effective normal stress and a shear stress across the circumference of the XCC single pile. It is suggested that XCC single piles have a higher efficiency in terms of material saving compared with CCC single piles.

1 INTRODUCTION

In order to improve the bearing capacity of a single pile, it is necessary to either increase its side resistance, end resistance or both [1]. By manipulating the cross-sectional geometry of a pile, its cross-sectional perimeter can be increased without increasing the cross-sectional area (material waste), which, in effect, alters the side resistance. Many studies have been conducted on the behaviour of special cross-sectional piles, such as the barrette [2], the belled pile [3], the pipe pile [4-5], the large diameter cast-in-place pipe pile [6], the tapered pile [7], and the H pile [8-9]. These piles alter the cross-sectional shapes that are designed to achieve the same objective, which is improving the pile performance, particularly the bearing capacity.

In recent years a new cross-sectional-shaped pile, the X-section cast-in-place concrete (XCC) pile, has been implemented in China (see Fig. 1). Since 2008, these new XCC piles, constructed as a piled raft system (including pile, gravel and/or geogrid), have been used to reinforce the soft ground for motorways in Nanjing, for example, two linkage sections between the expressway and the Fourth Bridge of the Yangtze River, two sections of the Jiangshan Street, and a section of the 312 National Motorway. The utilization of XCC piles in those projects has resulted in cost savings of more than 20%.

To advance these techniques, mainly for the design and construction of XCC piles, comparative field tests and three-dimensional (3D) numerical back-analyses between an XCC piled raft and a circular-section cast-in-place concrete (CCC) piled raft of the same cross-sectional area and configuration have been conducted by Lv et al. [10-12]. The results indicate that, under the same load conditions, approximately 66% and 46% of the applied load is carried by the XCC and CCC pile, respectively, and simultaneously, approximately 45% and 24% of the applied load is taken by the side resistance of the XCC and CCC pile, respectively. In other words, the larger bearing capacity of the XCC piled raft contributes to the cross-sectional geometry, leading to a larger pile perimeter and arching effects. In addition, a modified analytical solution, dependent on the cross-sectional geometry of XCC piles, was derived from the solution of Mindlin and Geddes by Lv et al. [13]. Corresponding parametric studies were conducted to explore the geometrical effects. In addition, the behaviour of the negative skin friction on the surface of XCC piles has been studied and reported by Kong et al. [14].

However, the stress-transfer mechanism of a single pile is quite different from that of a piled raft [15-17].
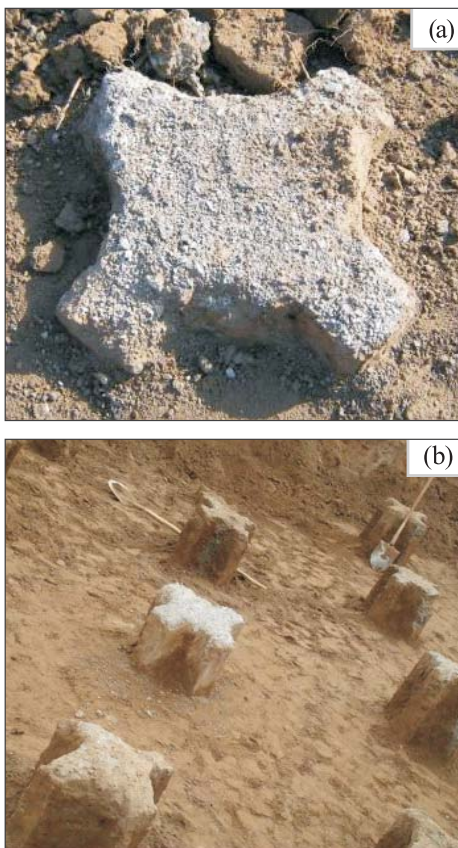
This is because the applied load is entirely carried by the pile for single piles, but it is carried by the piles and their surrounding soil for piled rafts. Nevertheless, the performance of XCC single piles, especially the stress-transfer mechanism between XCC single piles and their surrounding soil, is still not fully understood. This paper aims at revealing the fundamental stress-transfer mechanism for XCC single piles by field tests and 3D numerical back-analyses. For comparison, a CCC single pile of the same cross-sectional area is involved. The pile-soil interactions were considered by means of setting slip elements at the pile-soil interfaces.

2 BRIEF REVIEW OF XCC PILES

The cross-section and corresponding parameters of the XCC piles are shown in Fig. 2. The circle drown by the dashed line is defined as the surrounding circle and the arcs cutting into the surrounding circle at four symmetrical positions are defined as the cutting arc. The geometrical parameters of an X-shaped cross-section are $2a$, $2R$, θ, where $2a$ is the distance between two adjacent arcs; $2R$ is the diameter of the surrounding circle; and θ is the degree of the central angle of the cutting arcs. Thus, the radius of the cutting arcs r can be obtained by:

$$ r = \frac{(\sqrt{R^2 - a^2} - a)}{\sqrt{2}\sin\dfrac{\theta}{2}} \qquad (1) $$

For given geometrical parameters, the cross-sectional area of an XCC pile (A_X) is calculated as:

$$ A_x = \pi R^2 - 2\left[\theta\, r^2 - \sin(\theta)\, r^2\right] - $$
$$ -2\left[\left(\frac{\pi}{2} - 2\arcsin(\frac{a}{R})\right)R^2 - \cos\left(2\arcsin(\frac{a}{R})\right)R^2\right] \qquad (2) $$

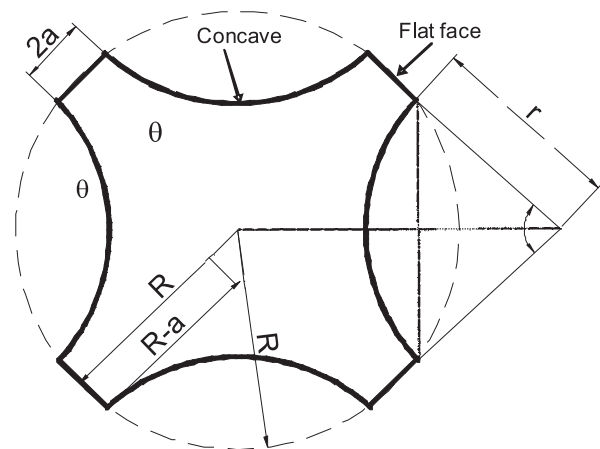**Figure 1**. Constructed: (a) XCC single pile, and (b) XCC pile group.

Figure 2. Cross-section and parameters of an XCC pile.

The cross-sectional perimeter of an XCC pile (C_X) is calculated as

$$C = 8\arcsin(\text{—})R + 4 \quad r \qquad (3)$$

The X-shaped cross-sections are formed to enlarge the pile perimeter by changing the directions of the arcs. Hence, ideally, the side resistance can be increased without decreasing the end resistance.

3 METHODOLOGIES

The performance of XCC single piles was studied using field tests and numerical simulations. Two field static load tests were conducted on an XCC single pile and a CCC single pile of the same cross-sectional area to explore the bearing capacity of XCC single piles. Meanwhile, corresponding 3D numerical back-analyses were carried out, not only to analyze the field tests but also to provide a deeper understanding.

3.1 Brief review of field static load tests

Two field static load tests were conducted in Nanjing, China. The XCC testing pile was cast in place using typical C20 concrete with dimensions of $2R = 0.53$ m, $2a = 0.11$ m, $\theta = 130°$ and a pile length (L) = 10.5 m, giving a cross-sectional area of 0.112 m^2 (Eq. 2). As a reference, a CCC single pile with the same cross-sectional area (pile diameter $D = 0.38$ m) was produced. Thus, the perimeters of the XCC cross-section and the CCC cross-section are 1.93 m and 1.19 m, respectively (Eq. 3). The perimeter of the XCC single pile is approximately 60% larger than that of the CCC single pile.

The site of the field tests is a relatively flat terrain. Original landscape features are retained and belong to the Yangtze River floodplain topography, according to the geomorphologic unit. The geotechnical properties of the soil profile are shown in Fig. 3. The ground-water table is located at a depth of approximately 2.2 m below the ground surface. Cone penetration tests (CPTs) were conducted to obtain the stiffness of the soil layers. The soil layer from the ground surface to a depth of approximately 3.5 m is soft; this is a fill layer. From a depth of 3.5 m to 8.0 m, the penetration resistance is more than 10 MPa, indicating a stiff fine sand layer. From a depth of 10.5 m to 20.0 m, the penetration resistance is approximately 7 MPa, suggesting a sand layer. Between the stiff fine sand and the sand layer, there is a soft inter-layer with a thickness of 2.5 m, which is silty clay. Some soil samples were retrieved for laboratory testing. The properties of the soil layers, including the water content, the unit weight, the effective friction angle, and the void ratio, are summarized in Table 1.

The test instrumentation consisted of the load apparatus and the detecting instruments. The load apparatus included a hydraulic jack and dial indicators. Different pressures, controlled by the load apparatus, were applied to the pile heads using a slow maintained load testing method. The pressure was read from the hydraulic table
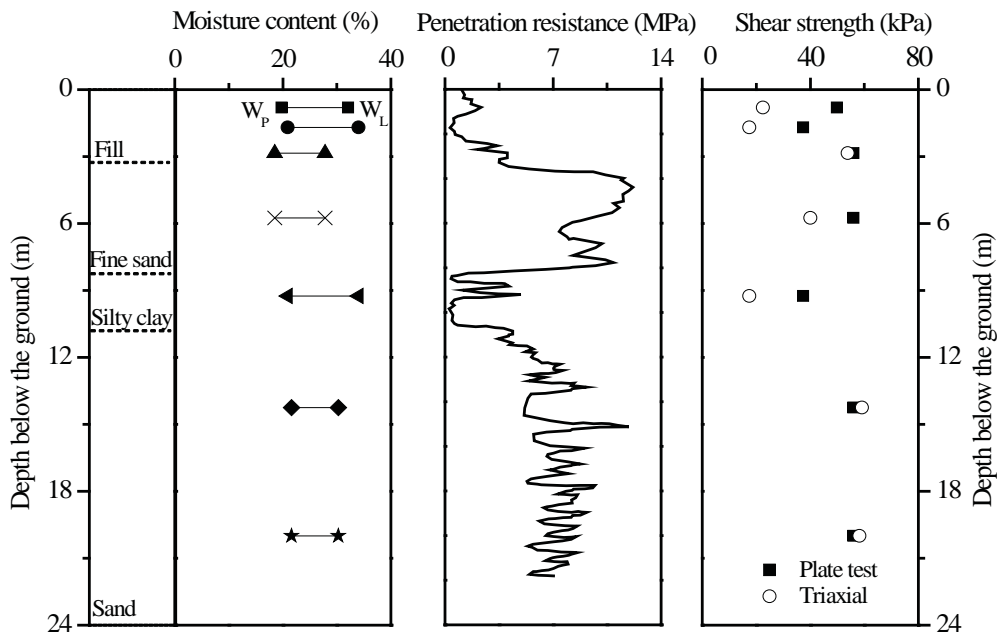

Figure 3. Soil layers and properties.

Table 1. Properties of the soil layers.

From /m	To /m	Type of soil	Mean water content /%	Void ratio	Unit weight /(kN/m^3)	Young's modulus /MPa	Cohesion */kPa	Effective friction angle /°
0.0	3.5	Fill	29.4	0.96	17.8	6	0	20
3.5	8.0	Fine sand	26.3	0.76	18.9	24	0	20
8.0	10.5	Silty clay	38.6	1.11	17.6	6	0	31
10.5	20.0	Sand	26.1	0.75	18.9	24	0	31

* denotes 1 Pa in ABAQUS

and the settlement was recorded using dial indicators with an accuracy of 0.01 mm. Each instrument was calibrated before the tests. More details about the field tests can be found in the literature [11].

3.2 Introduction of 3D numerical back-analyses

In this paper, 3D numerical back-analyses were carried out using the finite-element program ABAQUS [18]. For consistency, a full solid was simulated without taking advantages of the symmetry. In other words, the dimensions of the numerical CCC single pile and the numerical XCC single pile coincide well with those of the corresponding testing pile. Fig. 4a shows the meshes of the 3D pile foundations. Reduced integrated 8-node brick elements were created. Duplicated nodes were used to form a zero-thickness interface between the piles and their surrounding soil, as shown in Fig. 4b, adjacent to which the fine elements were generated. The interface friction angle (δ) was estimated using the equation proposed by Randolph and Wroth [19]:

$$\delta = \tan^{-1}[\sin\phi'\cos\phi'/(1+\sin^2\phi')] \qquad (4)$$

where ϕ' is the effective friction angle. The lateral earth-pressure coefficients (K_0) were estimated using the equation:

$$K_0 = 1 - \sin\phi' \qquad (5)$$

The external boundaries were positioned 5 m (approximately 13D) laterally from the center of the single piles and 20 m (approximately 1.9L) below the ground surface. Since the piles located at a distance of 6D or greater can be considered as a single acting pile [20], the distance chosen (13D) is deemed as sufficient to ensure no boundary effects. The boundary conditions are as follows: the radial curved plane was allowed to move freely in the tangential and z directions, but was fixed in the radial direction; for the bottom plane (i.e., z = 20 m), all of the movements were restrained.

A drained analysis was used in the numerical simulations. The piles (typical concrete) were simulated to be
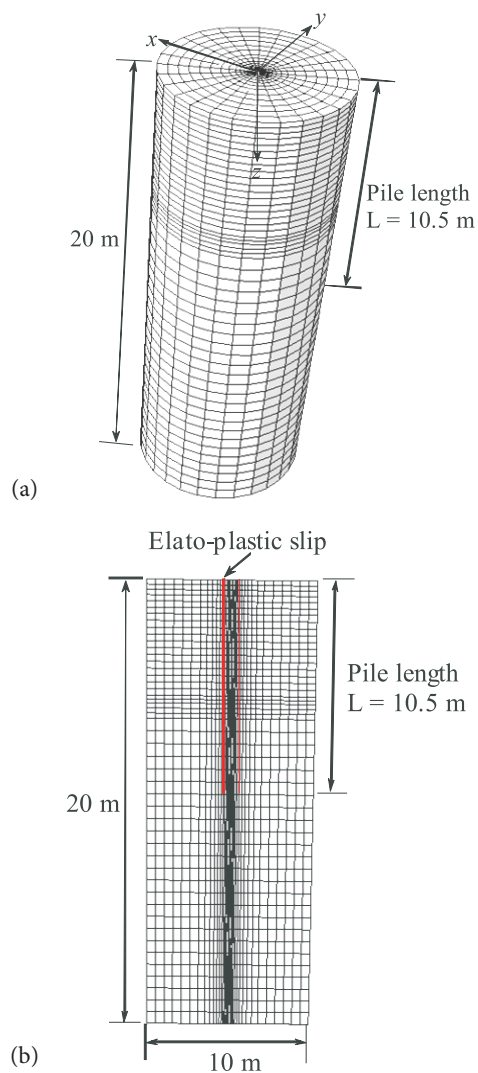

(a)

(b)

Figure 4. Finite-element mesh of: (a) 3D pile, and (b) elasto-plastic slip.

linear-elastic, with the Young's modulus being E_p (= 20 GPa) and the Poisson's ratio being v (= 0.2). The soil profile was simulated as an elasto-plastic material using the composite Mohr-Coulomb criterion. Fig. 5 shows the yield surface of the Mohr-Coulomb criterion [18]. The yield function is given by

$$F = R_{mc}q - p\tan\phi - c = 0 \qquad (6)$$

where p is the normal stress; q is the deviatoric stress; and $R_{mc}(\Theta,\phi)$ is a measure of the shape of the yield surface in the deviatoric plane and is defined as

$$R_{mc} = \sin(\Theta + \pi/3)\Big/(\sqrt{3}\cos\phi) + \cos(\Theta + \pi/3)\tan\phi/3 \quad (7)$$

where ϕ is the slope of the Mohr-Coulomb yield surface in the $R_{mc}q$-p stress plane, which is commonly referred to as the friction angle of the soils and ranges from 0 to 90°; c is the cohesion of the material; and Θ is the deviatoric polar angle, which is defined as

$$\cos(3\Theta) = r^3\Big/q^3 \qquad (8)$$

where r denotes the third stress invariant.

To eliminate the influence of apparent cohesion, the values of the cohesion for all of the soil layers were set to zero (1 kPa in ABAQUS). The effective friction angles were given according to the laboratory tests. The Young's moduli of the soil layers were estimated based on the CPT tests. The Poisson's ratios were taken to be 0.35 for all of the soil layers. The groundwater table was set at 2.2 m below the ground surface as the monitored results in field. The soil properties are summarized in Table 1.
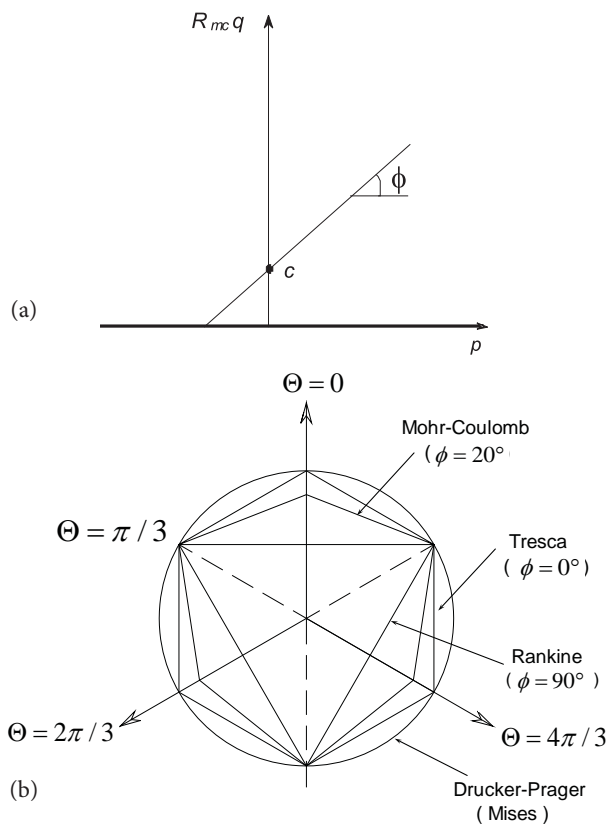
To simulate the static load tests, twelve steps including eight loading steps from P = 100 kN to 800 kN and four unloading steps from P = 800 kN to 0 kN were applied to the CCC single pile. A corresponding fifteen steps, including ten loading steps from P = 100 kN to 1000 kN and five unloading steps from P = 1000 kN to 0 kN, were applied to the XCC single pile. The load of each step was applied to the pile heads using linear amplitude.

4   RESULTS AND ANALYSES

4.1   Measured and computed load-settlement relationships

The measured and computed pile settlements versus the applied loads are shown in Fig. 6. Since the pile tips were located at the bottom sand layer, the measured settlement curves do not show a well-defined ultimate load. The computed settlement curves illustrate obvious elastic and plastic stages. The plastic stages of the CCC single pile and the XCC single pile start at approximately P = 220 and 310 kN, respectively. In addition, the computed settlement of the CCC single pile is underestimated during the loading stages. Meanwhile, the computed settlement of the XCC single pile is underestimated for the former loading stages, but overestimated for the latter loading stages. The differences between the measured and the computed results could be induced by overestimating the soil stiffness and idealizing the constitutive model. However, good agreements in the trend indicate the validation of the numerical back-analyses.

The ultimate bearing capacity that was adopted in this study was obtained using the settlement criterion s/D = 5% [21], where s denotes the pile settlement and D denotes the equivalent pile diameter. Hence, the

Figure 5. Yield surface of the Mohr-Coulomb criterion in: (a) the meridional plane, (b) the deviatoric plane [18].
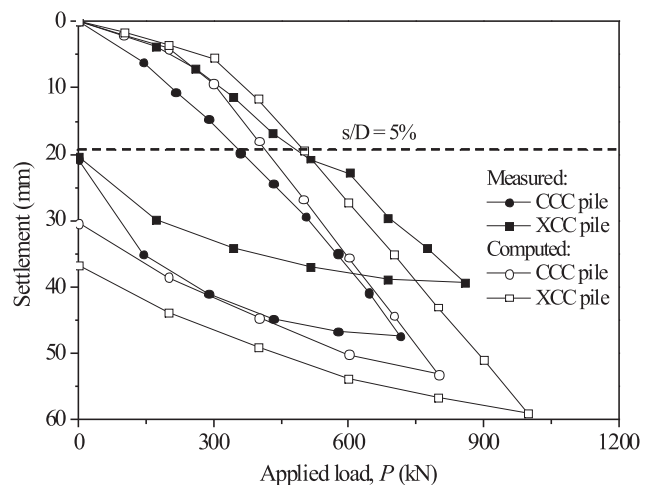
Figure 6. Measured and computed load-settlement relationships.

measured ultimate bearing capacities of the CCC single pile and the XCC single pile are $P = 350$ and 500 kN, respectively. Subsequently, using the same criterion, the computed ultimate bearing capacities of the CCC single pile and the XCC single pile are approximately $P = 400$ and 500 kN, respectively. It is obvious that the computed XCC single pile has an approximately 25% higher ultimate bearing capacity than the CCC single pile of the same cross-sectional area. In other words, XCC single piles have a higher efficiency in the cross-sectional area than the CCC piles. The contributions of the higher bearing capacity of the XCC piles will be explored step by step.

4.2 Load sharing between the side resistance and the end resistance

Fig. 7a and 7b show the computed axial forces of the CCC single pile and the XCC single pile, respectively. Both the CCC single pile and the XCC single pile have a similar trend, i.e., the axial force increases with an increasing applied load. Since the maximum loads of 800 kN and 1000 kN were applied to the CCC single pile and the XCC single pile in field tests, respectively, four loading steps (i.e., 200 kN, 400 kN, 600 kN, and 800 kN) are involved in the computed CCC single pile, and five loading steps (i.e., 200 kN, 400 kN, 600 kN, 800 kN, and 1000 kN) are included for the computed XCC single pile in this figure. Additionally, both the CCC single pile and the XCC single pile have another similar trend, i.e., the axial force decreases with the increasing depth. The axial force at the pile heads equals the applied load (P), while the axial force at the pile tips indicates the end resistance (Q_{end}). Therefore, the slope of the axial force is the unit side resistance and the difference between the applied load and the end resistance ($P–Q_{end}$) is the total side resistance. It was observed that

the slope of the axial force of the XCC single pile is smaller than that of the CCC single pile, demonstrating that the side resistance of the XCC single pile should be larger than that of the CCC single pile. In other words, the end resistance of the XCC single pile is smaller than that of the CCC single pile. This is because the XCC single pile has 60% more pile perimeter than the CCC single pile, although it has an identical cross-sectional area.

Based on the above description, the load sharing of the end resistance (α_{end}) and the side resistance (α_{side}) is obtained using Eq. 9 and Eq. 10, respectively. Fig. 8 shows the proportion of the load sharing of the side resistance and the end resistance with respect to the applied load. No matter what the cross-sectional shapes, α_{end} decreases with the applied load for the initial loading stages, but the trend becomes negative during the later loading stages, resulting in a minimum peak value at approximately $P = 300$ kN. Meanwhile, α_{side} increases with the applied load for the initial loading stages, but the trend becomes negative for the later loading stages, inducing a maximum peak value at the same load. This phenomenon is governed by the mobilization of the side resistance and the end resistance. It is found that during the initial loading stages, more than 80% of the applied load is carried by the end resistance. This indicates that the applied load is mainly resisted by the pile tips because the trend of the relative motion between the pile and soil has not been developed. Then, α_{side} exceeds 50% at approximately $P = 200$ kN. After the full mobilization of the side resistance (relative motion is approximately 5 to 10 mm) [22], α_{side} decreases, but α_{end} increases again. This is because the end resistance is fully mobilized at approximately $s/D = 5$%, which is always later than the full mobilization of the side resistance [22].
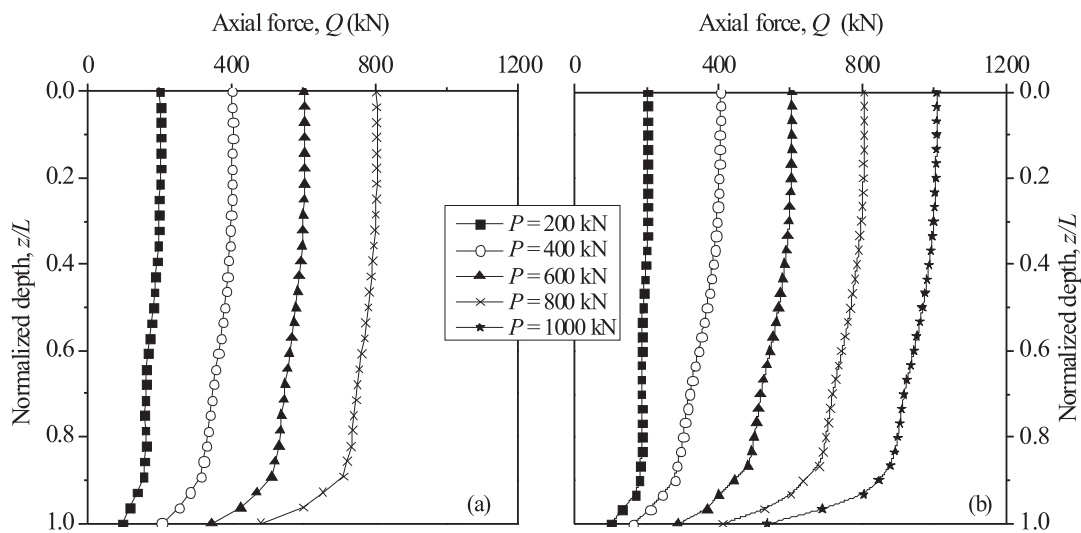

Figure 7. Computed axial force of: (a) CCC single pile, and (b) XCC single pile.
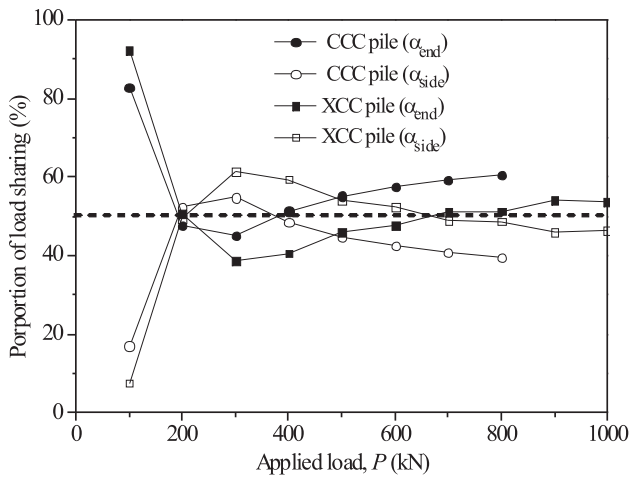
Figure 8. Computed load sharing of the side resistance and the end resistance.

$$\alpha_{end} = \frac{Q_{end}}{P} \qquad (9)$$

$$\alpha_{side} = 1 - \alpha_{end} = \frac{P - Q_{end}}{P} \qquad (10)$$

In addition, it was found that α_{side} is exceeded by α_{end} at $P = 400$ and 700 kN for the CCC single pile and the XCC single pile, respectively. This illustrates that the side resistance of the XCC single pile plays a more important role in resisting the applied load than the CCC single pile in serviceability conditions [22]. For example, α_{side} of the XCC single pile is always larger than that of the CCC single pile. The average side resistance of the XCC single pile is about 120% that of the CCC single pile.

4.3 Unit side resistance and total side resistance

In order to investigate the larger α_{side} of the XCC piles, the unit side resistance and the total side resistance at $P = 500$ kN are derived in Fig. 9a and 9b, respectively. In this study, the unit side resistance is back-calculated using the axial force. The total side resistance of a cross-section is obtained by the unit side resistance multiplied by the pile perimeter and the effective length of the segment. From the figure it is clear that the unit side resistance of the XCC single pile is smaller than that of the CCC single pile, especially for the lower part of the pile shaft. Below $z/L = 0.7$, the discrepancy between the two piles increases as the depth is increased. The unit side resistance of the CCC single pile is more than three times that of the XCC single pile at $z/L = 0.85$. Since the pile perimeter is normalized, the difference is caused by geometrical effects. After multiplying the unit side resistance by the pile perimeter, the total side resistance of the XCC single pile is about 120% that of the CCC single pile. This means that the pile perimeter plays an important role in improving the side resistance of XCC piles. The 60% higher pile perimeter induces an about 20% total side resistance, indicating that XCC single piles have a lower efficiency in the pile perimeter than the CCC piles.

To reveal the lower efficiency of the pile perimeter for XCC piles, the shear stress at different locations, i.e., X1, X2, X3, and X4, is derived and shown in Fig. 9c. As a reference, the shear stress estimated by the β-method [23] is also plotted in the same figure, including $\beta = 0.1$, 0.2, and 0.3. It was found that the shear stress developed on the concave surfaces of the XCC single pile (that can be described by $\beta = 0.28$) is larger than that developed
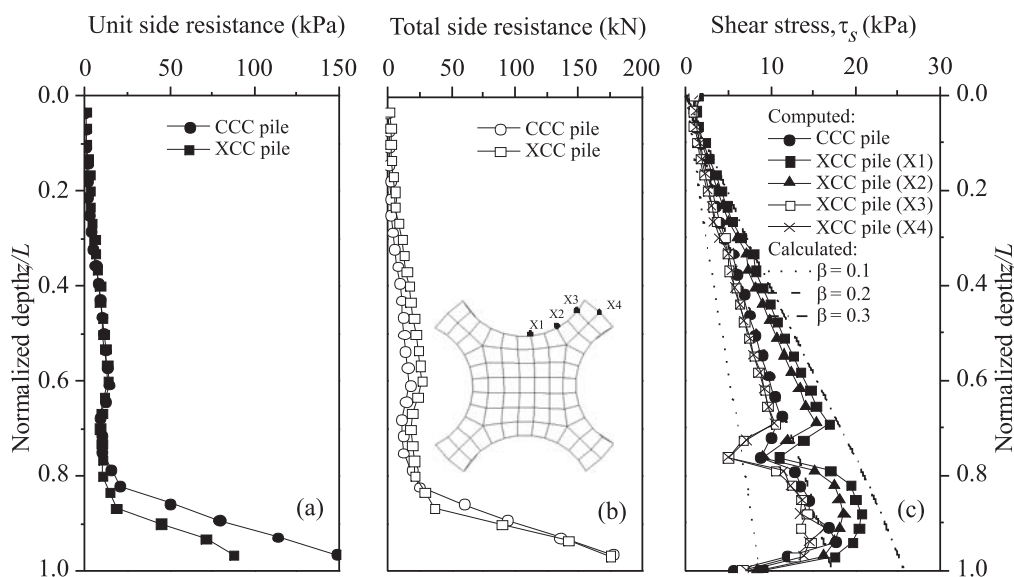

Figure 9. Computed: (a) unit side resistance, (b) total side resistance, and (c) non-uniform shear stress under $P = 500$ kN.

on the cylindrical surfaces of the CCC single pile (which can be described by $\beta = 0.20$), which is in turn larger than that developed on the outward flat surfaces of the XCC single pile (which can be described by $\beta = 0.18$). This observation provides two findings: firstly, for XCC piles, the β-method always overestimates the shear stress of the flat surfaces but underestimates the shear stress of the concave surfaces; secondly, the non-uniform shear stress induces a lower efficiency in the pile perimeter of the XCC single piles. In addition, at the intersection of the fill and fine sand ($z/L = 0.33$) and the fine sand and the silty clay ($z/L = 0.76$), the shear stress is unusual due to the special characteristics of the pile-soil interfaces.

4.4 Effective normal stress

Since the magnitude of the shear stress is closely related to the effective normal stress, the effective normal stress in the surrounding soil elements is derived on the basis of polar coordinates. Fig. 10 shows the effective normal stress distribution for the section $z/L = 0.5$ at $P = 500$ kN. It was found that the effective normal stress acting on the concave surfaces of the XCC pile is the largest of all sections, resulting in the largest shear stress at position X1 (see Fig. 9c). Meanwhile, the effective normal stress acting on the flat surfaces of the XCC pile is smaller than that on the cylindrical surface of the CCC pile and the concave surfaces of the XCC pile, resulting in a small shear stress of X4. This is because specific soil arching effects are developed across the circumference of the XCC piles, inducing stress redistribution. This is the fundamental reason for the larger ultimate bearing capacity of XCC single piles.

In order to illustrate the distribution of the effective normal stress along the depth, the effective normal stress acting on the pile shafts along the depth under $P = 500$ kN is shown in Fig. 11. Different locations, i.e., X1, X2,
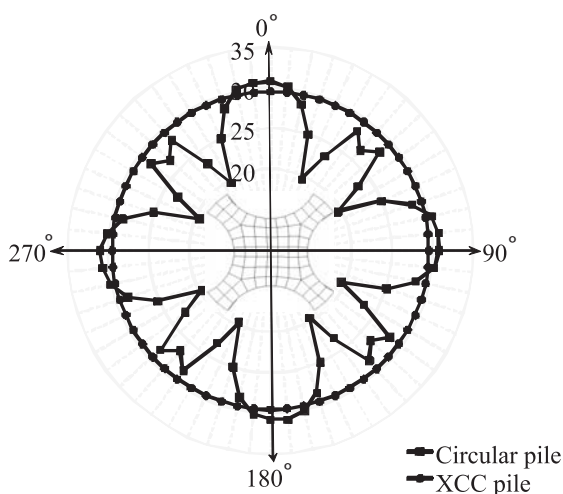
X3, and X4, are also involved. It was found that no matter whether it is the CCC single pile or the XCC single pile, the effective normal stress increases along the upper depth and then decreases along the lower depth. There are peak values at the intersections between two adjacent soil layers (i.e., $z/L = 0.33$ and 0.76). This trend agrees well with the distribution of the non-uniform shear stress (see Fig. 9c). Governed by the geometrical effects, the effective normal stress acting on X1 is the largest, but that acting on X3 is the smallest. In other words, the non-uniform shear stress on XCC pile shafts is induced by the non-uniform effective normal stress, which in turn results from the stress concentration and the principal stress rotation. There is an interesting phenomenon that the effective normal stress of X4 is obviously larger than that of X3, but the shear stresses of X3 and X4 are almost identical. This result demonstrates that the flat surfaces are easier to fully mobilize than the concave surfaces.
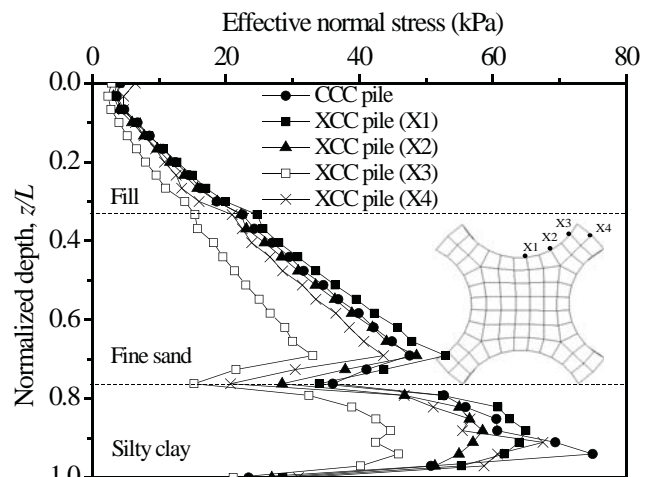
Figure 11. Computed effective normal stress along the depth under $P = 500$ kN.

5 CONCLUSIONS

Two field static load tests and the corresponding 3D numerical back-analyses were performed on an XCC single pile and a CCC single pile of the same cross-sectional area to investigate the performance of XCC single piles with respect to the geometrical effects. Based on the measured and computed load-settlement relationships, it is observed that the XCC single pile has an approximately 25% higher ultimate bearing capacity than the CCC single pile. This is mainly attributed to the geometrical effects of XCC piles, including a larger pile perimeter and a special stress-transfer mechanism, resulting in a large total side resistance.

Although the unit side resistance of the XCC single pile is slightly smaller than that of the CCC single pile under

Figure 10. Computed effective normal stress at $z/L = 0.5$ under $P = 500$ kN.

the same applied load, the total side resistance of the XCC single pile is approximately 120% that of the CCC single pile. This is caused by two opposite factors: firstly, the perimeter of the XCC single pile is approximately 160% that of the CCC single pile; secondly, the unit side resistance acting on the XCC single pile is smaller than that on the CCC single pile due to geometrical effects. A non-uniform effective normal stress was observed across the circumference of the XCC singe pile, leading to a non-uniform shear stress. Thus, the shear stress acting on the concave surfaces of the XCC single pile is larger than that on the cylindrical surface of the CCC single pile, which is larger than that on the flat surfaces of the XCC single pile. This is the special stress-transfer mechanism of XCC single piles, which is induced by soil arching effects around the X-shaped cross-section.

XCC single piles have a higher efficiency in the cross-sectional area (material saving) than CCC single piles of the same cross-sectional area since they have a higher bearing capacity. Meanwhile, XCC single piles have a lower efficiency in the cross-sectional perimeter than CCC single piles of the same cross-sectional area because the increment of the bearing capacity (25%) is smaller than the increment of the pile perimeter (60%).

Acknowledgement

REFERENCES

[1] Poulos, H.G., Davis, E.H. 1980. Pile foundation analysis and design. New York Wiley.

[2] Gifford, A.B., Green, G.E., Buechel, G.J., Feldman, A.I. 1986. In situ tests and design of a cylinder pile wall. Use of in situ tests in geotechnical engineering (GSP 6) (ASCE), New York, pp. 569–587.

[3] Ng, C.W.W., Yau, T.L., Li, J.H., Tang, W.H. 2001. Side resistance of large diameter bored piles socketed into decomposed rocks. Journal of Geotechnical and Geoenvironmental Engineering (ASCE) 127, 8, 642–657.

[4] Lee, J.H., Salgado, R., Paik, K. 2003. Estimation of load capacity of pipe piles in sand based on cone penetration test results. Journal of geotechnical and geoenvironmental engineering (ASCE) 129, 5, 391–403.

[5] White, D.J. 2002. An investigation into the behaviour of pressed-in Piles. PhD dissertation, University of Cambridge.

[6] Ding, X.M., Zheng, C.J., Liu, H.L. 2014. A theoretical analysis of vertical dynamic response of large-diameter pipe piles in layered soil. Journal of Central South University 21, 3327–3337.

[7] Ghazavi, M. 2007. Analysis of kinematic seismic response of tapered piles. Geotechnical and Geological Engineering 25, 1, 37–44.

[8] William, G.D., Thomas, S., Sarah, A., John, D., Christopher, L. 2010. Field-measured response of an integral abutment bridge with short steel H-piles. Journal of Bridge Engineering 15, 1, 32–43.

[9] Yang, J., Tham, L.G., Lee, P.K.K., Yu, F. 2006. Observed performance of long steel H piles jacked into sandy soils. Journal of Geotechnical and Geoenvironmental Engineering (ASCE) 132, 1, 24–35.

[10] Lv, Y., Ding, X., Liu, H. 2011. In-situ tests on cast-in-place concrete X-section pile for bearing capacity of single-pile composite foundation. Geotechnical Special Publication No. 220 ASCE, Changsha, 39–47.

[11] Lv, Y., Liu, H., Ding, X., Kong, G. 2012. Field tests on bearing characteristics of X-section pile composite foundation. Journal of Performance of Constructed Facilities (ASCE) 26, 2, 180–189.

[12] Lv, Y., Liu, H., Ng, C.W.W., Ding, X., Gunawan, A. 2014. Three-dimensional numerical analysis of the stress transfer mechanism of XCC piled raft foundations. Computer and Geotechnics 55, 365–377.

[13] Lv, Y., Liu, H., Ng, C.W.W., Gunawan, A., Ding, X. 2014. A modified analytical solution of soil stress distribution for XCC pile foundations. Acta Geotechnica 9, 3, 529–546.

[14] Kong, G., Zhou, H., Liu, H., Ding, X., Liang, R. 2014. A simplified approach for negative skin friction calculation of special-shaped pile considering pile-soil interaction under surcharge. Journal of Central South University 21, 3648–3655.

[15] Clancy, P., Randolph, M. F. 2001. Analysis of piled raft foundations using a variational approach. International Journal for Numerical and Analytical Methods in Geomechanics 17, 12, 849–869.

[16] Poulos, H.G. 2001. Piled raft foundations-design and applications. Géotechnique 50, 2, 95-113.

[17] Kalpakci, V., Özkan, M.Y. 2012. A simplified approach to the settlement estimation of piled rafts. Acta Geotechnica Slovenica 1, 77-85.

[18] ABAQUS standard user's manual, Ver. 6.6. 2006. Hibbitt, Karlsson & Sorensen. Inc., Pawtucket, R.I.

[19] Randolph, M.F., Worth, C.P. 1980. Application of the failure state in undrained simple shear to the shaft capacity of driven piles. Géotechnique 31, 1, 143-157.

[20] Lee, C.J., Chen, C.Z. 2002. Negative skin friction on ground piles. Proc. Int. Conf. Physical Modeling in Geotech., St. John's Newfoundland, Canada, 679-684.

[21] O'Neill, M.W., Reese, R.C. 1999. Drilled shaft: construction procedures and design methods. Federal Highway Administration, Washington, D.C.

[22] O'Neill, M.W. 2001. Side resistance in piles and drilled shafts. Journal of Geotechnical and Geoenvironmental Engineering (ASCE) 127, 1, 3-16.

[23] Meyerhof, G.G. 1976. Bearing capacity and settlement of pile foundations. Journal of Geotechnical and Geoenvironmental Engineering 102, 3, 197-227.